24 February 2023, A.Y: 2022 - 2023

Project on:

ANALYSIS OF ATMOSPHERIC DATA FOR MODELS OF THE ASTRONOMICAL SEEING

For the course of:

Astronomical Instrumentation

Author:

Jenny Frediani

Supervisor:

Gabriele Rodeghiero

Contents

1 Introduction **1**
1.1 Earth's atmosphere . . . 1
1.2 Astronomical Seeing . . . 2
1.3 Seeing measure techniques . . . 4
1.3.1 SODAR . . . 4
1.3.2 Meteorological balloons . . . 5
1.3.3 DIMM . . . 5
1.3.4 MASS . . . 6

2 Data analysis **7**
2.1 Dataset . . . 7
2.2 AXP model . . . 8
2.3 Samples of flights around Solstices . . . 8
2.4 $C_N^2(h)$ turbulence profile . . . 9
2.4.1 Signal filtering . . . 12
2.5 Local seeing . . . 14

Bibliography **19**

Chapter 1

Introduction

1.1 Earth's atmosphere

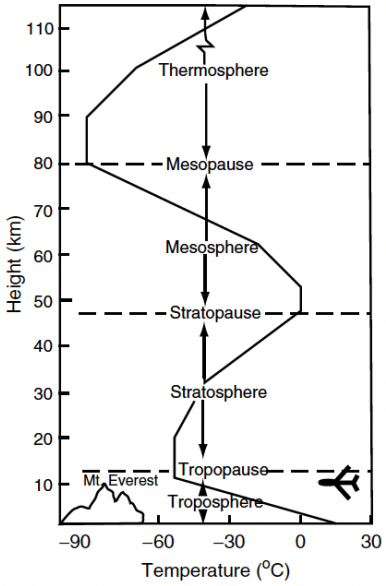

Figure 1.1: Average thermal structure of Earth's atmosphere. Figure adapted from: [3].

The atmosphere is the envelope which surrounds the Earth, and it contains several different chemical compounds in the form of gas and particulates. It is composed[1] primarily of Nitrogen N_2 (78.08%), Oxygen O_2 (20.98%), and Argon Ar (0.93%). There are also the so-called greenhouse gases - making up less than 0.1% of volume in dry atmosphere-, including Carbon Dioxide CO_2 (0.039%), Methane CH_4 (0.0017%), and Ozone O_3 (0.00006%). The solar radiation (that peaks in the visible band, according to the *Wien's law*), passes through the atmosphere and, apart from a small fraction that is reflected back to space, reaches the Earth's ground, which re-radiates it in the form of infrared (IR) radiation[2]. Much of this long wave radiation is trapped near the surface by the greenhouse gases, keeping the Earth an average temperature of about $+15°C$, warm enough to sustain life as we know it.

The amospheric pressure and the density, therefore the atmospheric temperature, decrease with altitude above the Earth's surface, because the atmosphere gets progressively rarefied and the IR irradiance by the Earth diminishes.

The atmosphere is vertically stratified in temperature in four main layers, each layer grading in the adjacent one as indicated in **Figure 1.1**. We shall focus here on the Troposphere, since the light coming from an object in the sky goes through all the atmospheric layers down to the Tropopause, which defines the smooth transition from the Troposphere to the Stratosphere, almost unperturbed. In other words, the atmospheric turbulence, which originates the astronomical *seeing* (see **Sec. 1.2**), mainly develops in the first 20 km of height above the Earth's ground; beyond the Tropopause, the air density declines exponentially, the turbulence starts to be optically negligible, and the energy transfer between gas volumes becomes less efficient.

The Troposphere represents the lowest atmospheric layer, in direct contact with the Earth ground, and extending up to a mean altitude of 13 km. It contains 75% of the mass of the atmosphere, and it is where clouds and weather occur. This layer is heated from the bottom by the convective motions in the

[1] Considering the average composition of the atmosphere below 25 km. The concentration of the chemical components is expressed as volume percentage in dry air.

[2] The peak wavelength associated to the black-body spectrum of the Sun is: $\lambda_\odot = 2897/T_\odot = 0.5012$ μm. For the Earth it is instead: $\lambda_\odot = 2897/T_\oplus = 11.361$ μm.

atmosphere, IR radiation from Earth's surface, and by a latent heat flux. The latter consists of the heat released during the evaporation of the water at the surface, resulting in air parcels which rise and cool down (building up the cooling gradient visible in **Figure 1.1**), in a way that the water vapor condenses and forms clouds and precipitation.

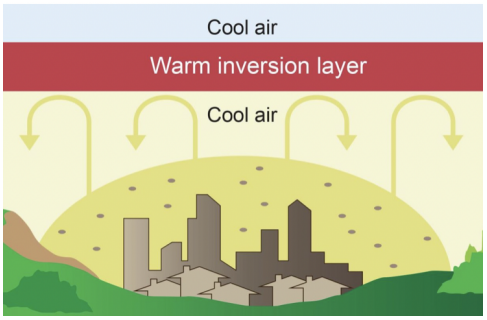

Figure 1.2: Cartoon representation of an inversion layer. Credits: ***engineeredfiltrationsystems.com***

Within the average thermal structure of the atmosphere, we shall distinguish between the local and temporary inversion layers, and the permanent inversion layers. The former generally subtend the turbulence layers: most of the atmospheric turbulence is in fact confined to specific, narrow, layers that are either close to inversion points of the temperature or that are interested by strong wind shears generating turbulence. The permanent inversion layers, instead, are relatively stable over time, at least in height, and can damp vertical air motions, since, as illustrated in **Figure 1.2**, these layers are warmer than the surrounding ones. This is due to, for example, the local orography of the ground, that introduces mechanical turbulence by wind shear mechanisms. It is worthwhile for the following discussion to introduce one particular atmospheric permanent inversion layer: the *ground layer*, which is the closest turbulence layer to the Earth's surface, caused by the combination of a temperature inversion layer, wind velocity gradient, land orography, and local meterological phenomena.

1.2 Astronomical Seeing

Ground-based astronomical observations in the visible and in the IR bands are mainly limited by the seeing effect, which affects the telescope spatial resolution and the optical system throughput[3].
The seeing is the degradation of the image of a point-like source in the sky onto the science instrument detector, due to the fact that the incoming wavefront of the source must cross the Earth's atmospheric turbulence layers before reaching the telescope. The seeing manifests in general as a broadening of the *Point Spread Function* (PSF), that is the distribution of the light intensity in the image of a given point-like source. The seeing originates from the temperature fluctuations affecting the local index of refraction of the atmosphere, therefore changing the direction of the light passing through it.
The index of refraction depends on the air density and on its chemical composition, according to the *Cauchy's formula*:

$$n - 1 = \frac{77.6 \times 10^{-6}}{T} \left(1 + 7.52 \times 10^{-3} \lambda^{-2}\right) \left(P + 4810 \frac{\nu}{T}\right) \tag{1.1}$$

where λ is the wavelength, P the pressure exerted by the atmosphere ($mbar$), T the atmospheric temperature (K), and ν the water vapor pressure ($mbar$). Fluctuations in humidity are not usually relevant to the seeing at astronomical sites, same for pressure fluctuations. Thus, the refractive index, and so the seeing, are mainly affected by temperature fluctuations. These fluctuations result from the natural convection or the mechanical turbulence that induce turbulent mixing of the atmospheric layers, that are characterized by different temperatures. The fluctuations in the index of refraction are therefore related to the structure of thermal turbulence in the atmosphere. In particular, the convection is practically limited to the layers below the Tropopause, while the mechanical turbulence manifests throughout the whole atmosphere, and it is associated to regions of high wind shear. The energy spectrum of the turbulence, referred as *Kolmogorov spectrum*, can be divided into three ranges, as shown in **Figure 1.3 (a)**. The thermal fluctuations occur in the central one (the inertial sub-range), where the spatial variation of the temperature has a spectrum $\propto k^{-5/3}$, with k being the *wave number* (inverse of a wavelength), i.e. the spatial frequency of the turbulence spectrum. The Kolmogorov spectrum can be expressed with a statistical *structure function* D_T, that corresponds, in this context, to the *temperature*

[3]The *etendue* is a fundamental property of an optical system, that can be defined in two dimensions as the product, which must be constant, between the area of the telescope entrance pupil and its subtended solid angle.

structure function $D_T(r)$, namely, the (averaged) variance over a span r of the temperature field $T(x)$:

$$D_T(r) = < (T(x+r) - T(x))^2 > = C_T^2 \; r^{2/3} \tag{1.2}$$

where C_T^2 is referred as the *constant of fine structure of the atmosphere*. Therefore, the atmospheric turbulence is quantified by measuring the difference in T between two points separated by a distance r. Regardless, the turbulence vertical profile (as a function of the altitude h) is parametrized by the *index of refraction structure index* $C_N^2(h)$:

$$C_N^2(h) = C_T^2(h) \; \left[77.6 \times 10^{-6} \; (1 + 7.52 \times 10^{-3} \; \lambda^{-2}) \; \frac{P(h)}{T(h)^2} \right]^2 \tag{1.3}$$

The C_N^2 index profile does not show a monotonic behaviour as a function of the altitude: as illustrated in **Figure 1.3 (b)**, and as we describe in **Sec. 2.4**, there are evident bumps corresponding to different turbulence layers.

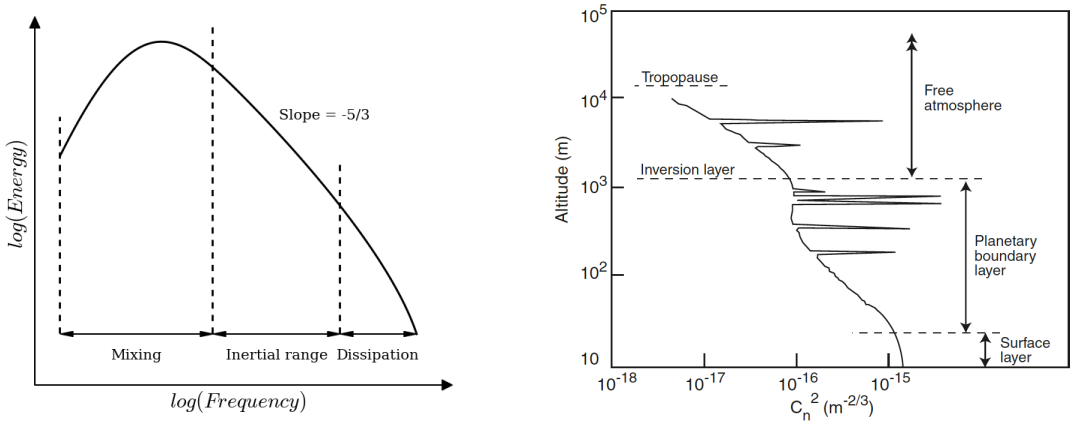

(a) The Kolmogorov spectrum. **(b) Representative turbulence profile of $C_N^2(h)$.**

Figure 1.3: (a) Figure adapted from [8]. (b) Figure adapted from [1].

The seeing profile originating from the atmospheric turbulence can be described using a single parameter, the so-called *Fried radius* r_0, which is related to $C_N^2(h)$ by:

$$r_0 = \left[1.67 \; \lambda^{-2} \; (cos\gamma)^{-1} \; \int C_N^2(h) \; dh \right]^{-3/5} \tag{1.4}$$

where γ indicates the zenith angle. The Fried radius, in practice, quantifies the size of an optically coherent air bubble with a homogeneous index of refraction. Thus, the image quality depends only on the integral of the C_N^2 index over the light path covered in the atmosphere. Another characteristic variable of the seeing that we can define is the apparent angle on the sky subtended by r_0, called *isoplanatic angle* θ_0, i.e. the angular distance within which two sources in the sky are affected by the same atmospheric turbulence. It can be expressed as a function of $C_T^2(h)$ as[4]:

$$\theta_0 = 0.94 \; \left[\int C_T^2(h) \; dh \right]^{3/5} \tag{1.5}$$

or, as a function of r_0, like:

$$\theta_0 \simeq 0.6 \; \frac{r_0}{h} \tag{1.6}$$

where h refers to the main turbulent layer above the telescope. Finally, we shall introduce also the characteristic time of atmospheric turbulence, the so-called *coherence time*, τ_0:

$$\tau_0 \simeq \frac{r_0}{v_{wind}} \tag{1.7}$$

which is the crossing time of a coherent air bubble of diameter r_0 over the line of sight, given the wind speed v_{wind} at the height where the main turbulence takes place.

[4]The multiplicative factor in the formula is obtained by assuming a vertical direction, a $\lambda = 500 \; nm$, and the typical conditions of the astronomical mountain sites, that is, a pressure of 770 $mbar$ and a temperature of $10°C$.

1.3 Seeing measure techniques

In this section we are going to review some of the methods that are used to estimate the seeing at the astronomical sites. Remote sensors, like the *SOnic Detection and Ranging*, or SODAR (**Sec. 1.3.1** below) instruments, and in situ measurements, as for radiosonde systems carried aloft by meteorological balloons (**Sec. 1.3.2**), allow to scan, layer by layer, the turbulence structure of the air column above the ground. Differential measurement methods (which exploit instruments that can be seen as remote sensors), like the *Differential Image Motion Monitor*, or DIMM (see **Sec. 1.3.3**), and the *Multi-Aperture Scintillation Sensor* (MASS; described in **Sec. 1.3.4**), provide, instead, an integrated measure of the seeing over the atmospheric column above the instrument, losing the information about the position of the atmospheric turbulent layers that originate the seeing. Yet, this kind of methods involves only parameters that are directly measurable, and the calibration procedure is mainly based on estimating the instrumental noise and the system limitations.

1.3.1 SODAR

The SODAR is a technique to measure the wind speed, the direction, and the turbulence parameters from the back-scattered acustic waves that get scattered back to the ground by fluctuations of the air density. The time of flight of these pulses determines the height of the turbulent eddy causing the back-scatter. Larger density fluctuations of the atmosphere imply higher turbulence, thus, the back-scatter strength is proportional to the turbulence. Nevertheless, in order to process this strength into the values of $C_T^2(h)$ and $C_N^2(h)$, which are related by[5]:

$$C_N^2(h) = \left[\frac{80 \times 10^{-6}\ P(h)}{T(h)^2}\right]^2\ C_T^2(h) \tag{1.8}$$

an estimate and a calibration of the variation of the temperature with the altitude are required.
Given that the air motion causes the returning signal to be Doppler shifted, this frequency shift is proportional to the wind speed in the direction of the sound wave. In particular, when the target (a turbulent eddy) is moving towards the SODAR instrument, the frequency of the returned signal is higher than the frequency of the transmitted signal. Conversely, when the turbulent eddy is moving away from the instrument's line of sight, the frequency of the returned signal is lower. The SODAR transmits a sound beam straight up (along the vertical), as well as at angles slightly off the vertical, to get a 3D wind velocity map. The meteorological data are typically averaged over vertical layers with a depth of $45 - 75\ m$. The wind data, in particular, are typically averaged over 5 to 100 m intervals. In units of time, the averaging interval is usually of the order of $15 - 60\ min$. By measuring the intensity and the frequency of the returned signal as a function of time after the transmitted sound pulse, we can determine the thermal structure and the radial velocity of the atmosphere at varying distances from the transmission antenna of the SODAR instrument.
A *mono-static* SODAR system uses the same antenna for transmitting and for receiving, so that the air scattering is associated to the temperature fluctuations alone, while a *bi-static system* (whose example is shown in **Figure 1.4**) uses separate antennas, adding the wind velocity fluctuations to the basis of the measurement.

Figure 1.4: A three antenna SODAR for wind and turbulence profile measurements up to 1000 m above ground. Figure adapted from [4].

[5]The temperature T is assumed to be in K, the pressure P in $mbar$, plus an index of refraction for light with a wavelength in the visible range.

1.3.2 Meteorological balloons

Weather balloons, inflated with Helium (see **Figure 1.5**), can be used to carry aloft a radiosonde sounding system to measure the vertical profiles of the C^2 indices, as well as of the atmospheric pressure, temperature, humidity, wind speed, and wind direction through dedicated sensors.
The temperature is typically measured using a small rod or a bead thermistor; the altitude of the balloon is determined using thermodynamic variables or adopting satellite-based *Global Positioning Systems* (GPS); the wind speed components (horizontal and vertical ones), and the wind direction, are estimated by measuring the position of the radiosonde relative to the Earth's surface as the balloon ascends. In particular, we measure the temperature structure function associated with the turbulence, $D_T(r)$ (defined in **Sec. 1.2**), so that $C_T^2(h)$ and $C_N^2(h)$ can be derived always from **Eq. (1.8)**, given the average pressure P $(mbar)$ and the average temperature T (K). The vertical resolution of the sensors is approximately ~ 5 - $6\ m$. The radiosonde also includes some electronic subsystems that sample each sensor at regular intervals of 2 to 5 s, and transmit the data to a ground-based receiver and data acquisition system.

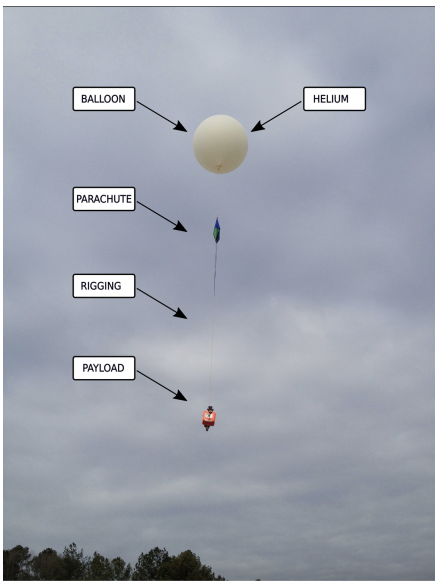

Figure 1.5: General layout of a meteorological balloon. Credits: ***basicairdata.eu***

1.3.3 DIMM

The DIMM represents a standard and widely used method of measuring the astronomical seeing. In the last few years, some valuable variations of the DIMM have been designed, such as the SHIMM (*Shack-Hartmann* DIMM) and the DIMM instrument built for the *Telescopio Nazionale Galileo* (the TNG-DIMM), but the basic working idea remains the same.
The seeing is estimated from the variance $\sigma^2(d)$ of the differential image motion of a source, as caught by two small circular apertures -of diameter D-, that are spatially selected through a mask in the entrance pupil plane of the telescope (see **Figure 1.6 (a)** for a schematic illustration in the upper right panel); the two images of the target get separated by placing a wedge prism over one of the sub-apertures. With such a setup is possible to realize an image of the two sources whose relative motion represents local wavefront distortions. The variance $\sigma^2(d)$, as observed over a distance $d \geq 2D$ between the two sub-apertures, can be split in a longitudinal $\sigma_l^2(d)$ and a transverse $\sigma_t^2(d)$ component:

$$\sigma_l^2(d) \simeq 2\ \lambda^2\ r_0^{-5/3}\ \left[0.179 D^{-1/3} - 0.0968\ d^{-1/3}\right] \tag{1.9}$$

$$\sigma_t^2(d) \simeq 2\ \lambda^2\ r_0^{-5/3}\ \left[0.179 D^{-1/3} - 0.145\ d^{-1/3}\right] \tag{1.10}$$

The differential motion is measured independently in these two directions, so, by reversing these formulas we retrieve two independent estimates for the seeing, that reduces the statistical error and captures the direction-dependent errors. The measurements are obtained at an average cycle frequency of 5 Hz, and $\sigma_l^2(d)$ and $\sigma_t^2(d)$ are calculated on $200 - 300$ short exposures of $5 - 20\ ms$ on average, roughly corresponding to a statistical estimate of the seeing every minute. At the end of each exposure, the variance of the relative motion and the intensity are evaluated to compute the seeing and the *scintillation index*. This index is defined as the normalized variance of the source intensity distribution on the image plane. In fact, the *scintillation* effect, that consists of the image intensity variations due to the atmospheric turbulence, strongly affects the images of the DIMM due to the small size of the sub-apertures. Their relative large separation in the pupil plane is responsible for decorrelating the intensity levels of the two images. A DIMM is only sensitive to wavefront perturbations on scales comparable to the distance between the two sub-apertures: if the turbulent layer moves considerably during the single exposures, the variance of the positions of the source is underestimated, leading to an underestimation of the seeing. At the same time, the differential nature of the DIMM measurement realizes a robust technique with respect to the vibrations induced by the wind shake, and the telescope tracking errors.

1.3.4 MASS

The MASS technique, sketched in **Figure 1.6 (b)**, can reconstruct 6-layer profiles of the atmospheric turbulence at fixed altitudes (with low vertical resolution $dh/h \sim 0.5$), by correlating the scintillation patterns of an isolated bright star in four concentric annular apertures of outwardly increasing diameters from 2 cm to 8 cm. This configuration sets the sensitivity of the MASS to the cm scales on the telescope pupil plane. The spatial structure of the scintillation pattern produced by the turbulence at a height z is of the order of the *Fresnel radius* $r_F = \sqrt{\lambda\, z}$, meaning that the scintillation speckle contains information on the distance to the turbulent layers originating the seeing effect. The four pupil beams are then directed to four *photomultipliers*, which count the incoming photons with an exposure time of 1 ms. This series of photon counts is used to compute, every second, ten *scintillation indices* s^2 (SIs), i.e. variance and covariance of the intensity normalized by the square of the average intensity. A linear relation between the SIs and the vertical turbulence profile C_N^2 holds:

$$s_k^2 = \int W_k(z)\; C_N^2(z)\; dz \tag{1.11}$$

where the *weighting function* (WF) describes the altitude response of a given aperture or a given aperture combination k, depending on the wavelength and the aperture size. Knowing the WFs, the SIs are fitted to a model of six turbulent layers at fixed altitudes of 0.5, 1, 2, 4, 8, and 16 km, allowing to restore the turbulence profile at those heights. Combined with a DIMM, this technique also allows to estimate the ground-layer seeing, that is produced in the first 0.5 km above the observing site, by subtracting the turbulence integrals measured with the DIMM and the MASS.

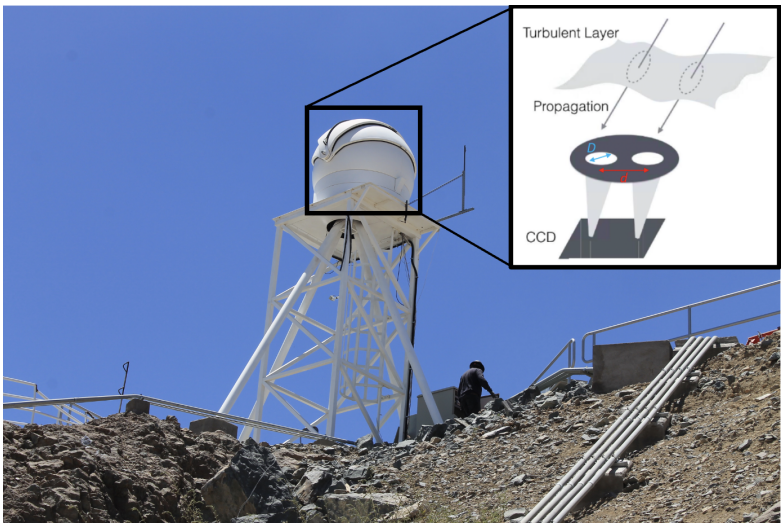

(a) DIMM instrument installed at the AURA Vera C. Rubin Observatory, under construction on Cerro Pachón (Chile).

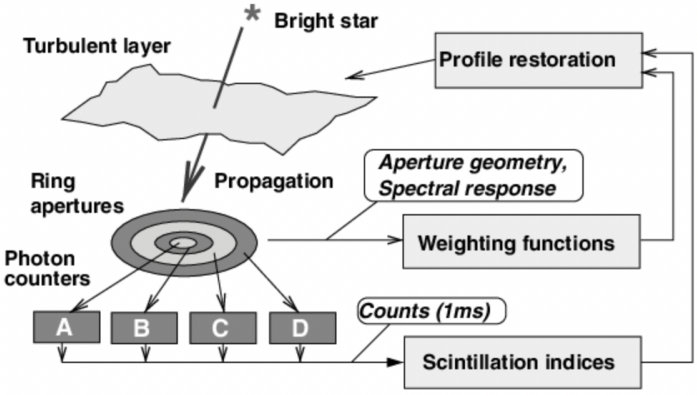

(b) Illustration of the MASS technique.

Figure 1.6: (a) Credits: *Rubin Obs./NSF/AURA*. (b) Figure adapted from [18].

Chapter 2

Data analysis

The main goal of this project is to derive the $C_N^2(h)$ profile and an estimate of the local seeing at the *Concordia* site according to the so-called *AXP model* described in [19], by analyzing a set of meteorological data obtained with the balloon radiosonde system of the *'Routine Meteorological Observation at Station Concordia'* collaborative project between the *Institut Polaire Français* (IPEV), and the *Programma Nazionale di Ricerche in Antartide* (PNRA)[1].

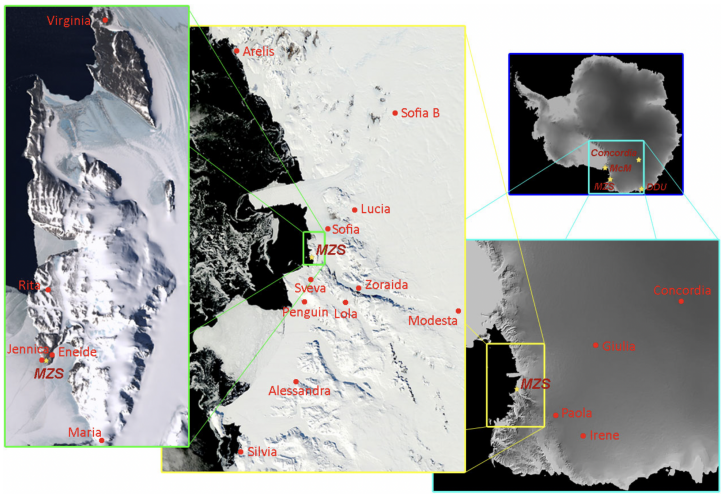

Figure 2.1: Map of the Automatic Weather Stations (AWS) managed by the Osservatorio Meteo-Climatologico Antartico. Credits: climantartide.it

2.1 Dataset

The dataset for this project came as a large text file storing in different columns: the date and the hour of launch (in *Coordinated Universal Time*, UTC) of the balloons, the duration of the flight (in s; 2800 s on average for our selected sample around the winter solstice, 4600 s on average for the sample around the summer solstice), the height reached by the balloons (in m), the atmospheric temperature (in $°C$; we converted it into K for all the following calculations), the atmospheric pressure (in $mbar$), the relative level of humidity (%), the wind speed (in m/s), and the wind direction. The measurements have been obtained from the Station Concordia (highlighted in the cyan box in **Figure 2.1**), located at the *Dome C* in the Antarctic plateau (South Pole). The balloon, Helium-inflated, carries a *VAISALA RS41* radiosonde, and it rises with a velocity of $\sim 5\ m/s$ up to a maximum height between 15 and 30 km before exploding. As reported in the first column of our dataset, at the Station Concordia only one launch per day (at 12 UTC) is performed for the entire solar year. The data have being collected since 2005; in this project we decided to analyze the dataset of 2022. It has been shown that the Dome C (3250 m in altitude) constitutes an advantageous site for astronomical observations, thanks to the low infrared sky emission (10 to 100 times lower than from any mid-latitude site), the high percentage (75%) of cloud-free time, and the low atmospheric precipitable water vapour, aerosol and dust content

[1] climantartide.it

of the atmosphere. Moreover, at this site there is evidence of a very low ground layer ($< 220\ m$ above the surface level), topped by a stable *free atmosphere*, slow wind speeds, and the absence of seismic activity.

2.2 AXP model

As anticipated, for our data analysis we take advantage of the AXP model proposed by [19], which is based on the statistical study of 162 profiles of meteorological balloons (from different campaigns performed between 1990 and 2002 from sites located both in the Northern and the Southern Emispheres) equipped with microthermal sensors. This model is able to provide a vertical profile of the C_N^2 index with a 1 km vertical resolution, and that is linked to the gradient of the *mean potential temperature* $\theta(h)$. This function is defined as the temperature of an air parcel which adiabatically adjusts at a standard pressure of 1000 $mbar$:

$$\theta(h) = T(h)\ \left(\frac{P(h)}{1000}\right)^{-0.286} \tag{2.1}$$

so that in the boundaries of a turbulent atmospheric layer, in which the turbulence mixes the air, the potential temperature tends to an equilibrium state. Consequently, the gradient of the potential temperature becomes larger, producing peaks of $C_N^2(h)$ at the edge of every shear layer. From this evidence, the structure function of the temperature fluctuation $C_T^2(h)$ should follow a median value $\langle C_T^2\rangle(h)$, calibrated by the absolute value of the vertical gradient of the mean potential temperature[2]:

$$C_T^2(h) = \langle C_T^2\rangle(h)\left[A(h)\left|\frac{d\theta}{dz}\right|(h)\right]^{p(h)} \tag{2.2}$$

where the power index $p(h)$ is introduced to regulate the amplitude of the peaks, while the function $A(h)$ $[m\ K^{-1}]$ is used to correct the level of these peaks. We have taken the coefficients ($p(h)$, $A(h)$, $\langle C_T^2\rangle(h)$) required by the model to calculate the C_T^2 index from *Table 2* of [19]; they are evaluated in bins of 1 km altitude[3], from 0 up to 30 km above the ground. In solving **Eq. (2.2)**, we had to take a particular precaution to evaluate $\left|\frac{d\theta}{dz}\right|(h)$: in fact, it happens that the balloon floats around the same height a couple of times, implying in those cases a gradient to be evaluated over a null dz bin. In order to deal with this problem, we first took the mean temperature and the mean pressure between the two consecutive grid points of equal height, then we removed the first of these two grid points from the dataset, and we arrived at the gradient of the potential temperature by taking the derivative of **Eq. (2.1)** once inserted in it the evaluated mean temperature and the mean pressure. Once obtained $C_T^2(h)$, the C_N^2 vertical profile can be derived from **Eq. (1.8)** entering this equation with the pressure P, and the temperature T supplied by the dataset; see **Sec. 2.4** for our results. Consistently with the authors, we computed the vertical gradient of the potential temperature at a resolution of 200 m, and we kept the same resolution to estimate the C^2 indices, but fixing the $p(h)$, $A(h)$, and $\langle C_T^2\rangle(h)$ coefficients at their tabulated value over each bin of increasing altitude in order to get $C_T^2(h)$ as modelled. The AXP model also provides a formula to estimate the local seeing (in radians) for layers of 1 km of thickness (h_i):

$$r_0(h_i) = 5.25\ \lambda^{-1/5}\left[\int C_N^2(z)\ dz\right]^{3/5} \tag{2.3}$$

Our results on this topic are summarized in **Sec. 2.5**.

2.3 Samples of flights around Solstices

In order to compute the vertical profile of the atmospheric turbulence in terms of C_N^2, and therefore retrieving an estimate of the seeing, we focused on two samples of 10 day flights around the winter and the summer solstice in the Southern Emisphere. In particular, we inspected the behaviour of the mean temperature, the mean pressure and of the wind velocity in the atmosphere as a function of the height above the surface (**Figure 2.3**), in order to verify that there were not missing/corrupted data, and that these atmospheric variables followed the expected trends. Predictably, the temperature drops down to

[2]Conforming to the authors, we excluded negative values of the gradient from our analysis, because these values occur in unstable convective regimes, which are regimes not supposed to follow their model.

[3]The value of 1 km is arbitrary, but, according to the authors, a smaller value could induce a loss of correlation, and a larger value a loss of performance for the model.

almost $-80°C$ in the antarctic winter (**Figure 2.3 (a)**), while relatively higher temperatures ($> -40°C$) are reached in the summertime (**Figure 2.3 (d)**). When comparing the two samples of the temperature profiles, as shown in **Figure 2.2**, it is clearly visible in both cases that a cooling gradient builds up from the launching height of the balloons (3.239 km above the ground) up to ~ 10 km, where the Tropopause lies (refer back to **Figure 1.1**) and a permanent inversion layer occurs. At higher altitudes, instead, and up to the maximum height reached by the sampled flights (< 30 km), corresponding to the bottom part of the Stratosphere, the atmospheric layers tend to be isothermal[4]. Yet, given the different solar illumination at the polar latitudes during winter and summer times, the sensed temperature increases again in the sampled flights around the summer solstice, while the opposite happens around the winter solstice day. The atmospheric pressure (see **Figure 2.3 (b)** and **Figure 2.2 (e)**) smoothly decreases in an exponential way according to the *hypsometric equation*:

$$P_2 = P_1 \exp\left(\frac{z_2 - z_1}{H}\right) \tag{2.4}$$

where P_2 and P_1 refer to the pressure exerted by the atmosphere respectively at an altitude z_2 and z_1 (with $z_2 > z_1$), while H[5] quantifies the scale height over which P decreases by a factor 1/e.
Finally, the vertical profiles of the wind velocity (**Figure 2.3 (c)** and **Figure 2.3 (f)**) show several fluctuations, which are stronger than in the case of the temperature profiles.

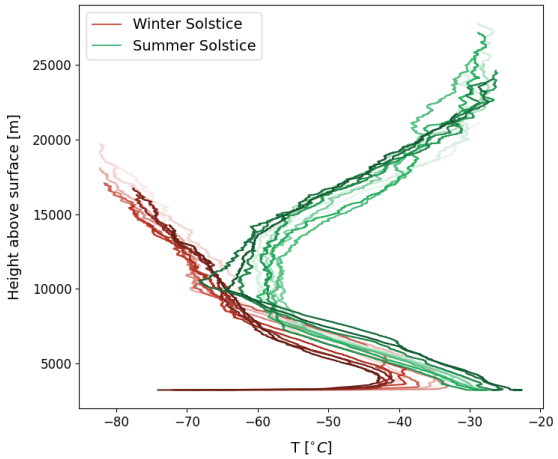

Figure 2.2: Comparison between the vertical profiles of temperature for winter flights (*red scale lines*) and summer flights (*green scale lines*).

2.4 $C_N^2(h)$ turbulence profile

Figure 2.4 first of all reports the vertical profiles of the $\left|\frac{d\theta}{dz}\right|$ function (**Figure 2.4 (a)-(d)**) and of the C_T^2 index (**Figure 2.4 (b)-(e)**). Starting from these two quantities, we computed the turbulence profile of the C_N^2 index (**Figure 2.4 (c)-(f)**) for the winter solstice and for the summer solstice day flights (shown here as the representative ones of the two samples). These three functions do not change monotonically with increasing altitude, and in general it is difficult to distinguish between the signal peaks and the noise because they are characterized by a similar profile both in profile amplitude, width and temporal frequency (in **Sec. 2.4.1** we describe how we tackled with this problem). What is in common between the $\left|\frac{d\theta}{dz}\right|$ and the C_N^2 profiles (given that they are correlated functions), and that represents the most reliable feature of these signals despite the noise, is the narrow, highest[6] amplitude peak visible around ~ 3000 m, which is related to the ground layer. The other peaks likely represent a mixture of noise and local higher altitude turbulence layers.

[4]Then, starting from ~ 25 km in altitude, where the Ozone gas mostly concentrates, the air starts to warm up again because of the photodissociation of the O_3 molecules induced by the UV solar radiation.

[5]It is defined as $H = \frac{k_B T}{mg}$, being m the mass of the molecule mixture, k_B the *Boltzmann constant*, T the temperature (assuming an isothermal atmosphere), and g the gravitational acceleration on Earth.

[6]This peak is effectively the highest in amplitude for the $\left|\frac{d\theta}{dz}\right|$, C_T^2, and the C_N^2 profiles recovered for the summer flights. The winter flights, instead, tend to display the highest amplitude content towards 20 km of altitude, which must be linked to higher noise level plus stronger T/v_{wind} fluctuations, hence stronger turbulence.

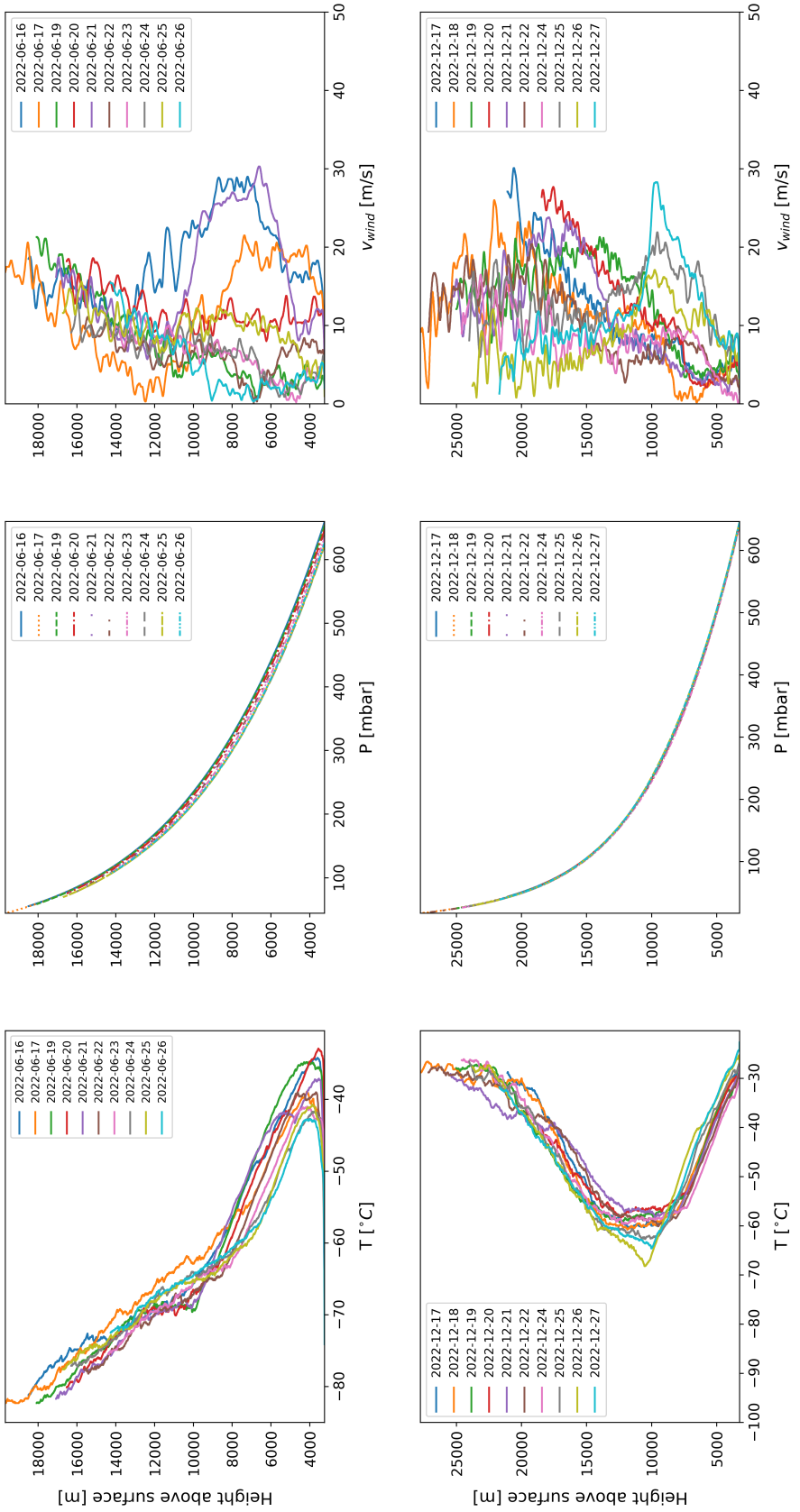

Figure 2.3: ***First row.*** **Vertical profiles of temperature (a),** ***left*****; pressure (b),** ***centre*****; wind velocity (c),** ***right*****; for a sample of 10 flights around the Antarctic Winter Solstice.** ***Second row.*** **Vertical profiles of temperature (d),** ***left*****; pressure (e)** ***centre*****; wind velocity (f),** ***right*****; for a sample of 10 flights around the Antarctic Summer Solstice.**

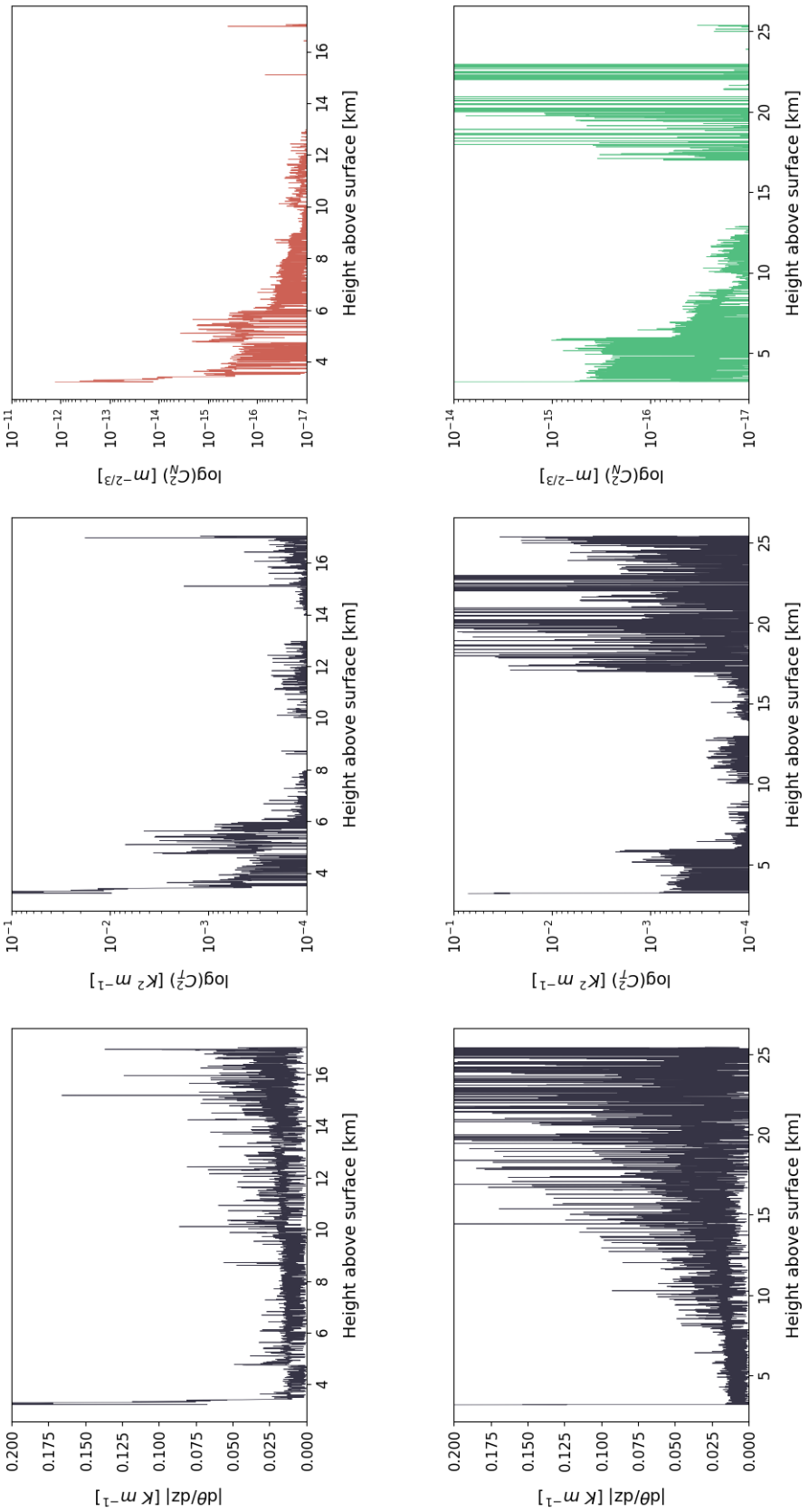

Figure 2.4: ***First row.*** **Vertical profiles of $\left|\frac{d\theta}{dz}\right|$ (a),** ***left*****; C_T^2 (b),** ***centre*****; C_N^2 (c),** ***right*****; for the Winter Solstice flight (2022-06-21).** ***Second row.*** **Vertical profiles of $\left|\frac{d\theta}{dz}\right|$ (d),** ***left*****; C_T^2 (e),** ***centre*****; C_N^2 (f),** ***right*****; for the Summer Solstice flight (2022-12-21). All curves have been cut in the y-axis at high altitudes for graphical reasons.**

2.4.1 Signal filtering

In order to get a more reliable and cleaner $C_N^2(h)$ profile, we implement a filter to remove the noise. Specifically, we filtered the $\left|\frac{d\theta}{dz}\right|(h)$ function with a low-pass *Butterworth filter* of order $n = 20$ and plug it into **Eq. (2.2)** to get in the end a filtered $C_N^2(h)$ profile.
The Butterworth filter is characterized by an amplitude response in the frequency domain of:

$$|H(jw)| = \frac{1}{\sqrt{1 + \left(\frac{\omega}{\omega_c}\right)^{2n}}} \tag{2.5}$$

where ω_c identifies the cutoff frequency of the filter and n the order of the filter (see **Figure 2.5 (a)**).

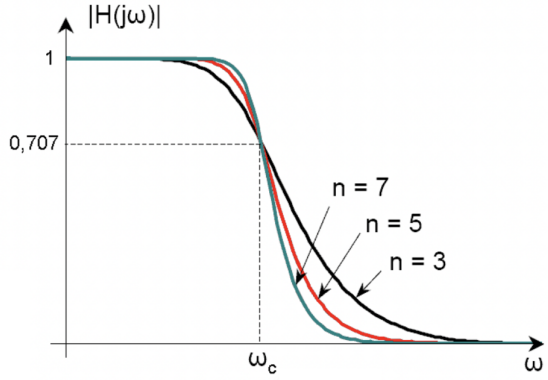

(a) Gain of Butterworth Low-pass Filter for different orders.

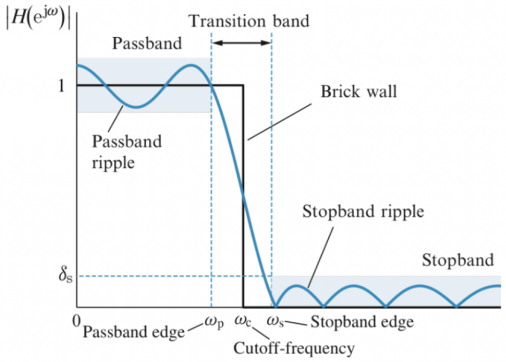

(b) Scheme of filter response characteristics.

Figure 2.5: (a) Figure adapted from [2]. (b) Credits: *cheap.com*

To select a suitable filter profile, we first look at the *Power Spectrum Density* (PSD) of the signal (in our case, the PSD of $\left|\frac{d\theta}{dz}\right|(h)$) to understand at which frequencies the harmonics of the signal lie, to keep them under the response curve of the filter and preserve the signal itself[7].

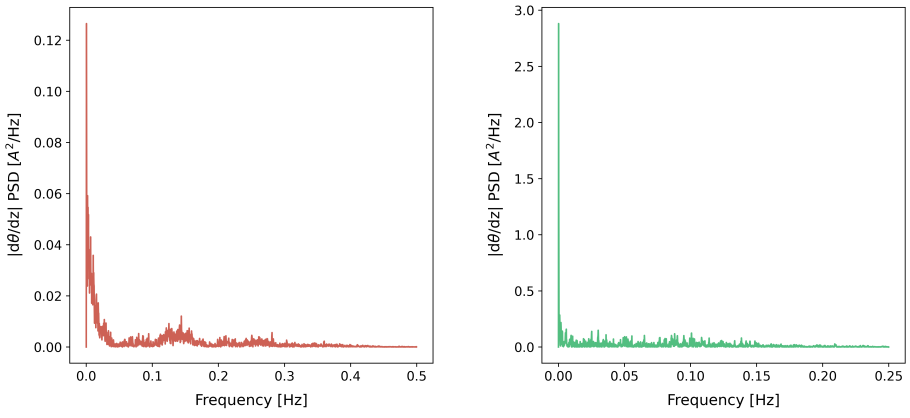

Figure 2.6: (a), *left*: PSD of $\left|\frac{d\theta}{dz}\right|(h)$ for Winter Solstice flight (2022-06-21). (b), *right*: PSD of $\left|\frac{d\theta}{dz}\right|(h)$ for Summer Solstice flight (2022-06-21).

From PSDs like those shown in **Figure 2.6 (a)-(b)**, we deduced that the predominant harmonic to be saved arises, predictably, near the ground layer, at low frequencies (this is way we opted for a low-pass

[7]Each frequency at which we find a peak in the PSD, indeed, corresponds to the inverse of the temporal interval of (ideally) equally spaced peaks in the profile of $\left|\frac{d\theta}{dz}\right|$ versus time of flight t, or equivalently versus height, since we know that the balloons ascend at ~ 5 m/s.

filter), whereas the noise tends to build up a long tail towards high frequencies. Thus, we decided the cutoff frequency ω_c of the filter (depending on the flight data, we have fixed $\omega_c = 0.07, 0.1, 0.2\ Hz$) accordingly to the location of the peaks of high amplitude in the $\left|\frac{d\theta}{dz}\right|$ vertical/temporal profile, which are the ones we want to keep in the filtered signal. For the order, instead, we always used $n = 20$, to get a sharp transition between the filter *passband* (where the filter holds the signal) and its *stopband* (where the filter cut off the signal; refer to **Figure 2.5 (b)**), because the signal and the noise peaks have similar frequencies. **Figure 2.7** and **Figure 2.8** report the vertical profiles of the $\left|\frac{d\theta}{dz}\right|$ function for the winter solstice and the summer solstice flights, before and after the application of the filter. In **Figure 2.7 (c)** and in **Figure 2.8 (c)**, in particular, it can be appreciated that in the filtered signals we managed to keep the high amplitude signal peaks, as well as the dampening of the underlying noise. Finally, in **Figure 2.9** and **Figure 2.10** we show the filtered C_N^2 profiles as a function of the altitude for the two representative flights of our samples. Having computed them for all flights, we used these filtered profiles to estimate the local seeing.

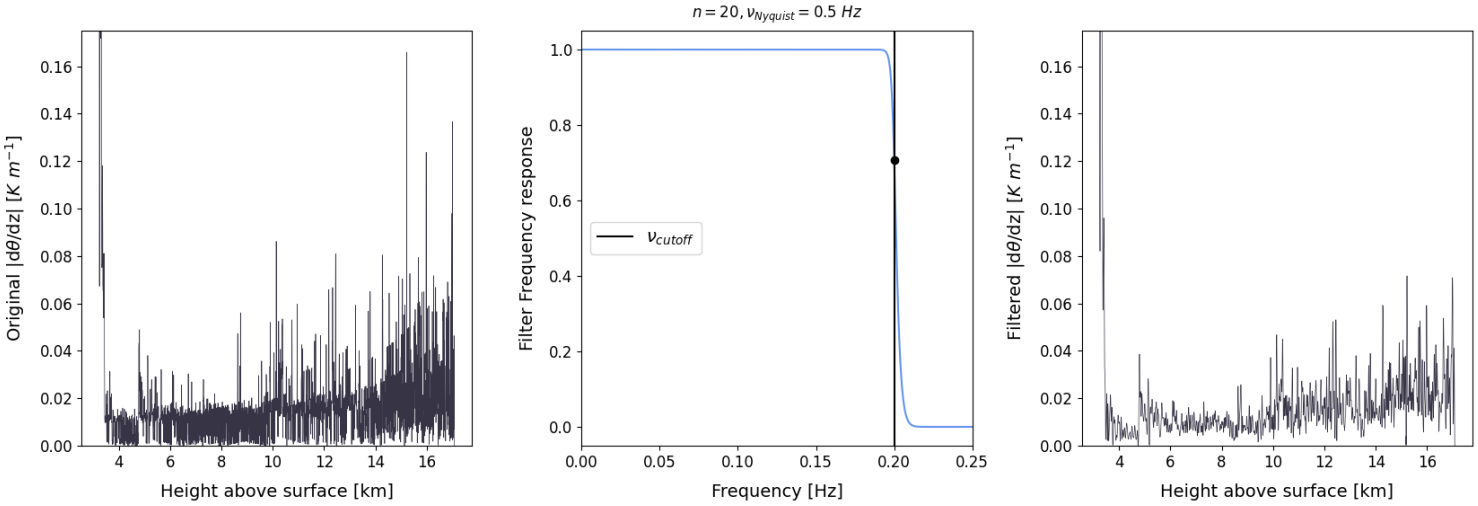

Figure 2.7: ***From left to right.*** **(a) Original $\left|\frac{d\theta}{dz}\right|(h)$ profile. (b) Butterworth Filter frequency response applied on $\left|\frac{d\theta}{dz}\right|(h)$. (c) Filtered $\left|\frac{d\theta}{dz}\right|(h)$ profile. The plots refer to the Winter Solstice flight (2022-06-21). Left and right curves have been cut in the y-axis at high altitudes for graphical reasons.**

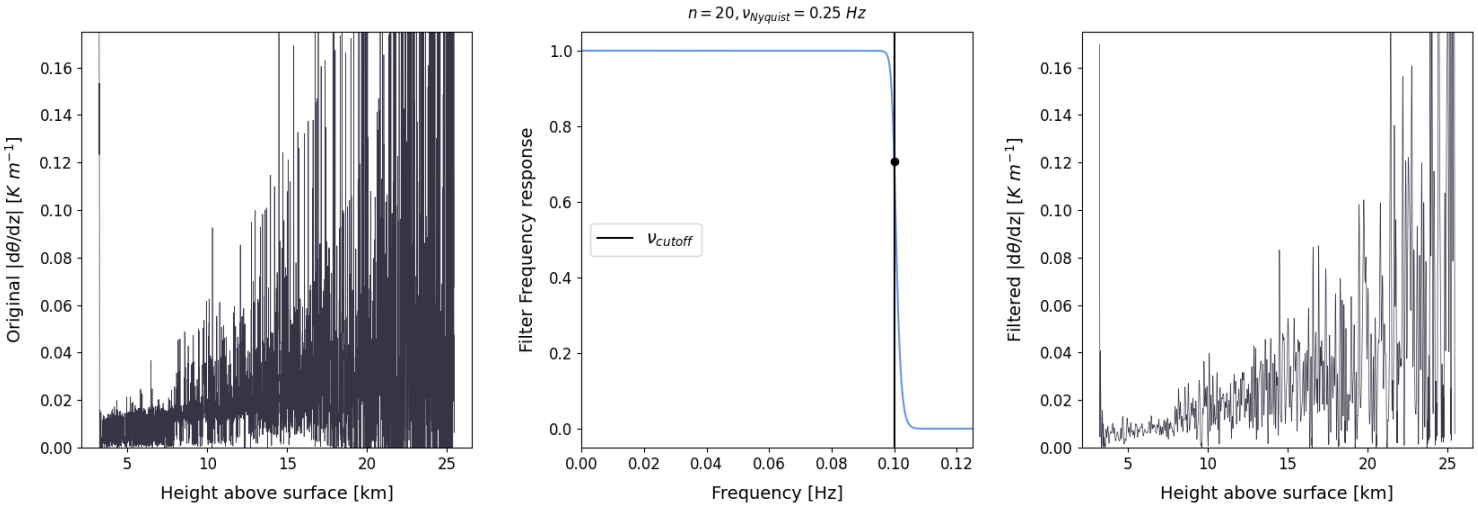

Figure 2.8: ***From left to right.*** **(a) Original $\left|\frac{d\theta}{dz}\right|(h)$ profile. (b) Butterworth Filter frequency response applied on $\left|\frac{d\theta}{dz}\right|(h)$. (c) Filtered $\left|\frac{d\theta}{dz}\right|(h)$ profile. The plots refer to the Summer Solstice flight (2022-12-21). Left and right curves have been cut in the y-axis at high altitudes for graphical reasons.**

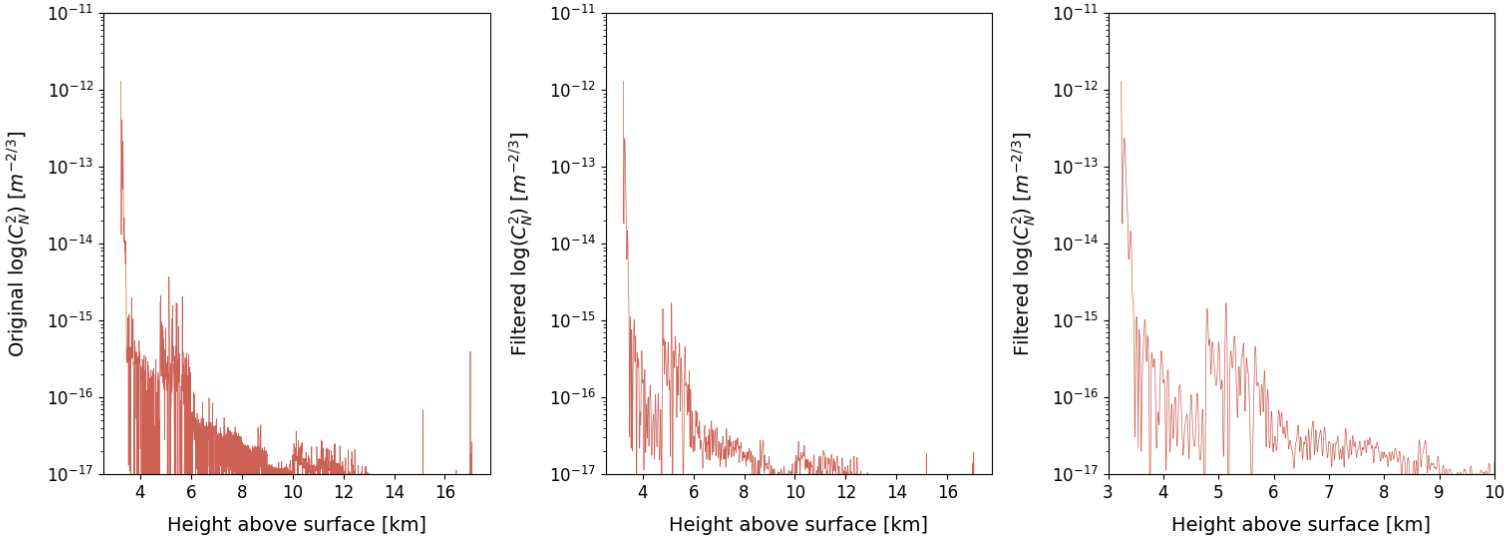

Figure 2.9: ***From left to right.*** **(a) Original $C_N^2(h)$ profile. (b) Filtered $C_N^2(h)$ profile. (c) Filtered $C_N^2(h)$ profile zoomed between 3 and 10 km of altitude. The plots refer to the Winter Solstice flight (2022-06-21).**

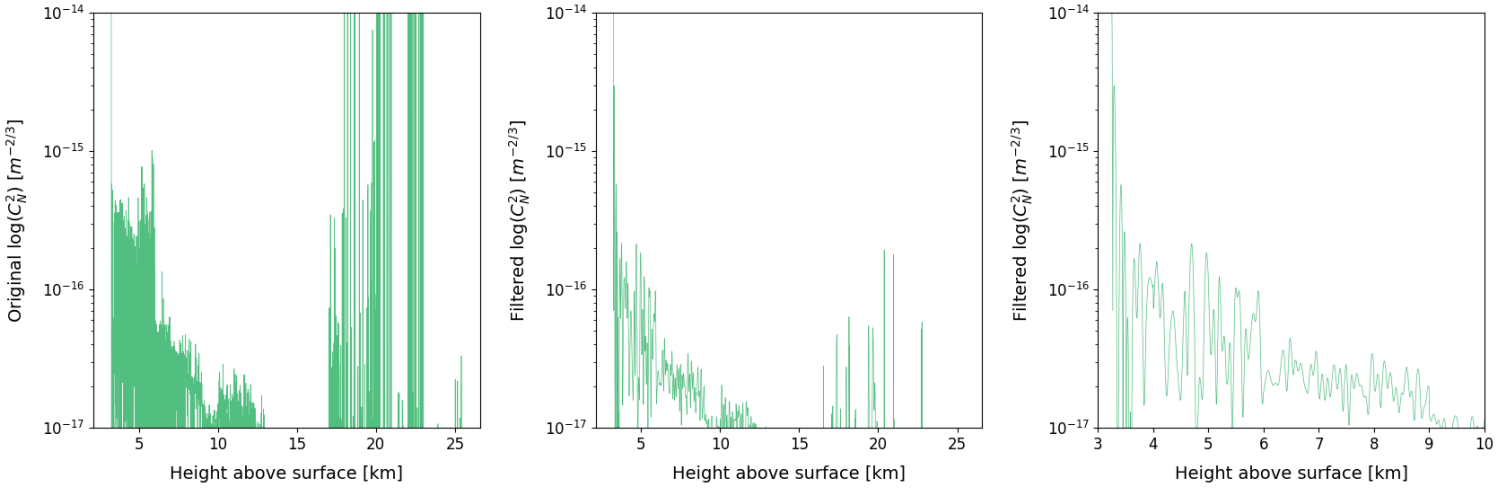

Figure 2.10: ***From left to right.*** **(a) Original $C_N^2(h)$ profile. (b) Filtered $C_N^2(h)$ profile. (c) Filtered $C_N^2(h)$ profile zoomed between 3 and 10 km of altitude. The plots refer to the Summer Solstice flight (2022-12-21). Left curve has been cut in the y-axis at high altitudes for graphical reasons.**

2.5 Local seeing

We computed the integral in **Eq. (2.3)** summing together the contributions from all the slices of height (~ 5 m thick each) sampled by each flight, fixing the wavelength in the formula to 0.5 μm, as indicated by the authors, and converting the resulting seeing estimates in arcseconds. In doing this, we encountered the following problem: in the very first ~ 260 m covered by each flight, the integral gives a very large seeing value, ranging from 4 to 12 arcsec (see **Figure 2.11 (a)**), while, for the bins at higher altitude and of 1 km thickness, the r_0 results to be around 1 arcsecond or smaller.
We therefore decided to calculate the r_0 values also excluding from the integration the first 1 km of sensed altitude (3239 - 4000 m), obtaining, as shown in **Figure 2.11 (b)**, seeing estimates closer to the expected values.

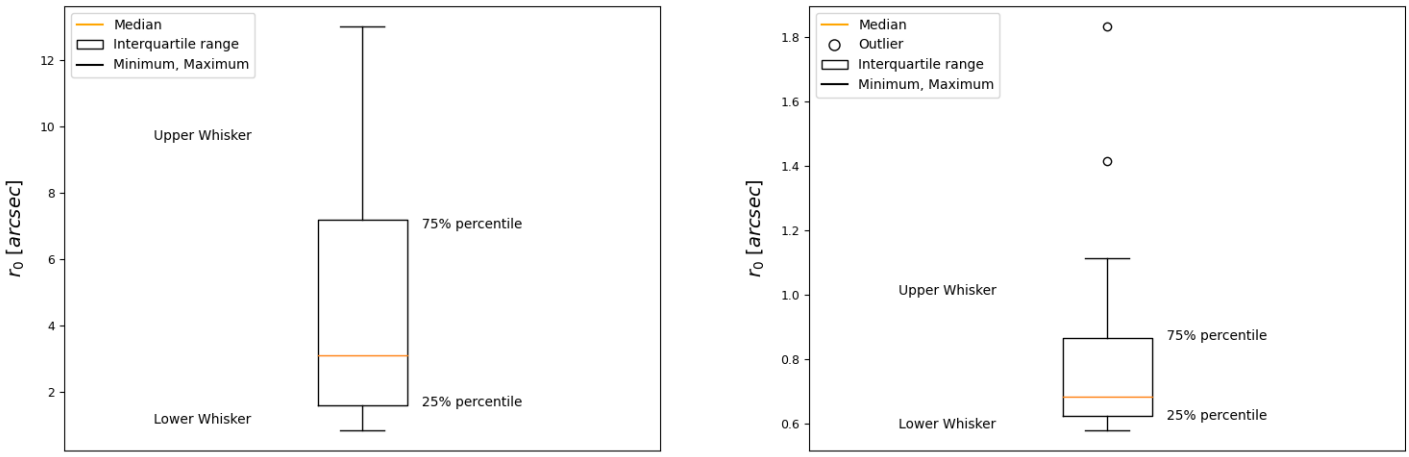

Figure 2.11: Cumulative r_0 values distribution for all sampled winter and summer flights integrating above the ground from 3 km (a), *left*; from 4 km (b), *right*.

Sounding of	r_0 [3239 m -] (arcsec)	r_0 [4000 m -] (arcsec)
2022-06-16	5.164	1.112
2022-06-17	3.038	0.735
2022-06-19	5.547	0.984
2022-06-20	7.850	0.642
2022-06-21	7.015	0.857
2022-06-22	6.171	0.724
2022-06-23	13.012	0.670
2022-06-24	7.768	0.580
2022-06-25	7.648	0.610
2022-06-26	8.737	0.640
2022-12-17	2.341	1.415
2022-12-18	1.201	0.616
2022-12-19	1.164	0.893
2022-12-20	2.431	1.832
2022-12-21	1.314	0.800
2022-12-22	1.654	0.579
2022-12-24	3.147	0.680
2022-12-25	0.835	0.627
2022-12-26	1.701	0.686
2022-12-27	1.435	0.608

Table 2.1: Cumulative r_0 values computed for all sampled winter and summer flights.

In **Table 2.1** are listed our computed values of r_0 in arcseconds, flight by flight, that we combined all together to produce the boxplots in **Figure 2.11**.
For comparison, in [7], observations carried out between 23 March and 5 May 2004 of the wintertime seeing from the Dome C, combining the measurements from the MASS and the SODAR techniques, resulted in a median seeing of 0.27 arcsec.
According to [19], instead, the seeing distribution estimated by the AXP model ranges from 0.5 to 3.5 arcsec (with a median value of 1.13 arcsec), with the largest seeing values coming from the South Pole campaign of 1995.
As a final mention, in [9], a seeing estimate from the surface level at the South Pole was obtained by launching 16 balloon flights equipped with the microthermal sensors designed by the authors plus a Vaisala radiosonde between 20 June and 18 August 1995, resulting in a median seeing (averaged over 15 balloon flights) of 1.6 arcsec.
Yet, our seeing estimates can be directly compared only to those reported in [7], since, as for us, and differently from the other two cited works, their data have been collected at the Dome C site.
Putting things in perspective, our median seeing values of 3.093 arcsec (orange line, **Figure 2.11 (a)**) and 0.683 arcsec (orange line, **Figure 2.11 (b)**), are in reasonable good agreement with theirs (0.27 arcsec), taking into account the main limitations of our work: *(i)* we exploited a model (the AXP model) not tested with data collected at the Dome C site; *(ii)* the AXP model, where tested, provides a large scatter in the seeing distribution; *(iii)* our dataset came with only one temperature measurement, instead of a finer mean temperature averaged with two values sensed at 1 m distance as commonly used for seeing measurements.

Bibliography

[1] Y. Pierre Bely. *The Design and Construction of Large Optical Telescopes*. English. Springer New York, 2003. ISBN: 9780387955124. DOI: 10.1007/b97612.

[2] M. Bogdan and M. Panu. "LabVIEW modeling and simulation, of the digital filters". In: *2015 13th International Conference on Engineering of Modern Electric Systems (EMES)*. 2015, pp. 1–4. DOI: 10.1109/EMES.2015.7158411.

[3] III Stuart F. Chapin, A. Pamela Matson, and M. Peter. Vitousek. *Principles of Terrestrial Ecosystem Ecology*. Springer, 2011. ISBN: 1441995021.

[4] Stefan Emeis. *Surface-Based Remote Sensing of the Atmospheric Boundary Layer*. English. Springer, 2012. ISBN: 9789400733213.

[5] U.S. ENVIRONMENTAL PROTECTION AGENCY (EPA). *Meteorological Monitoring Guidance for Regulatory Modeling Applications*. URL: https://www.epa.gov/sites/default/files/2020-10/documents/mmgrma_0.pdf.

[6] G. Thomas Farmer and John Cook. *Climate Change Science: A Modern Synthesis: Volume 1: The Physical Science*. English. Vol. 1. Springer, 2013. ISBN: 9789400757578. DOI: 10.1007/978-94-007-5757-8.

[7] Jon S. Lawrence et al. "Exceptional astronomical seeing conditions above Dome C in Antarctica". In: *Nature* 431.7006 (Jan. 2004), pp. 278–281. DOI: 10.1038/nature02929.

[8] K. Arthur Lidtke. "Predicting radiated noise of marine propellers using acoustic analogies and hybrid Eulerian-Lagrangian cavitation models". PhD thesis. University of Southampton, 2017. URL: https://eprints.soton.ac.uk/413579/.

[9] R. D. Marks et al. "Measurement of optical seeing on the high antarctic plateau". In: *Astron. Astrophys.* 134 (Jan. 1999). Provided by the SAO/NASA Astrophysics Data System, pp. 161–172. DOI: 10.1051/aas:1999100. URL: https://ui.adsabs.harvard.edu/abs/1999A&AS..134..161M.

[10] Jack E. McCrae et al. "Comparison between SODAR and anemometer-based turbulence measurements". In: *Society of Photo-Optical Instrumentation Engineers (SPIE) Conference Series*. Ed. by Jean J. Dolne, Mark F. Spencer, and Santasri R. Bose-Pillai. Vol. 12239. Society of Photo-Optical Instrumentation Engineers (SPIE) Conference Series. Oct. 2022, 1223907, p. 1223907. DOI: 10.1117/12.2634206. URL: https://ui.adsabs.harvard.edu/abs/2022SPIE12239E..07M.

[11] Emilio Molinari et al. "The new TNG-DIMM: calibrations and first data analysis". In: *Ground-based and Airborne Telescopes IV*. Ed. by Larry M. Stepp, Roberto Gilmozzi, and Helen J. Hall. Vol. 8444. Society of Photo-Optical Instrumentation Engineers (SPIE) Conference Series. Provided by the SAO/NASA Astrophysics Data System. Sept. 2012, 844462, p. 844462. DOI: 10.1117/12.925900. URL: https://ui.adsabs.harvard.edu/abs/2012SPIE.8444E..62M.

[12] Hajime Ogane et al. "Atmospheric turbulence profiling with multi-aperture scintillation of a Shack–Hartmann sensor". In: *Monthly Notices of the Royal Astronomical Society* 503.4 (Apr. 2021), pp. 5778–5788. ISSN: 0035-8711. DOI: 10.1093/mnras/stab105. eprint: https://academic.oup.com/mnras/article-pdf/503/4/5778/37059213/stab105.pdf. URL: https://doi.org/10.1093/mnras/stab105.

[13] Saavidra Perera et al. "SHIMM: a seeing and turbulence monitor for astronomy". In: 9909 (2016). Ed. by Enrico Marchetti, Laird M. Close, and Jean-Pierre Véran, 99093J. DOI: 10.1117/12.2231680. URL: https://doi.org/10.1117/12.2231680.

[14] Gabriele Rodeghiero. *Fundamentals of Adaptive Optics – Lecture 1*. URL: https://virtuale.unibo.it/pluginfile.php/1477454/mod_resource/content/1/Lecture1-AT-AO.pdfl. Department of Physics and Astronomy, University of Bologna, 2022.

[15] M. Sarazin and F. Roddier. "The ESO differential image motion monitor". In: *Astronomy and Astrophysics* 227.1 (Jan. 1990). Provided by the SAO/NASA Astrophysics Data System, pp. 294–300. URL: https://ui.adsabs.harvard.edu/abs/1990A&A...227..294S.

[16] A. Tokovinin. "From Differential Image Motion to Seeing". In: *The Publications of the Astronomical Society of the Pacific* 114.800 (Oct. 2002). Provided by the SAO/NASA Astrophysics Data System, pp. 1156–1166. DOI: 10.1086/342683. URL: https://ui.adsabs.harvard.edu/abs/2002PASP..114.1156T.

[17] A. Tokovinin and V. Kornilov. "Accurate seeing measurements with MASS and DIMM". In: *Monthly Notices of the Royal Astronomical Society* 381.3 (2007), pp. 1179–1189. DOI: 10.1111/j.1365-2966.2007.12307.x.

[18] A. Tokovinin et al. "Restoration of turbulence profile from scintillation indices". In: *Monthly Notices of the Royal Astronomical Society* 343.3 (Aug. 2003), pp. 891–899. ISSN: 0035-8711. DOI: 10.1046/j.1365-8711.2003.06731.x. eprint: https://academic.oup.com/mnras/article-pdf/343/3/891/3904224/343-3-891.pdf. URL: https://doi.org/10.1046/j.1365-8711.2003.06731.x.

[19] Hervé Trinquet and J. Vernin. "A Model to Forecast Seeing and Estimate C2N Profiles from Meteorological Data". In: *Publications of The Astronomical Society of The Pacific - PUBL ASTRON SOC PAC* 118 (May 2006), pp. 756–764. DOI: 10.1086/503165.

[20] Hervé Trinquet and J. Vernin. "Using meteorological forecasts to predict astronomical 'seeing'". In: *Spie Newsroom* (Jan. 2009). DOI: 10.1117/2.1200906.1704.